Analysis of Hybrid Air Vehicles using Computational Fluid Dynamics

M. Carrión⋆, M. Biava⋆, R. Steijl⋆, G.N. Barakos⋆†, D. Stewart⋆⋆
⋆Computational Fluid Dynamics Laboratory, School of Engineering, University of Liverpool
Harrison Hughes Building, Liverpool, L69 3GH, U.K., e-mail: mcarrion@liverpool.ac.uk
⋆⋆Hybrid Air Vehicles Ltd.
Hangar 1, Cardington Airfield, Shortstown, Bedford, MK42 0TG
†Corresponding author

Abstract

This paper presents an aerodynamic study of bodies related to lighter than air vehicles, using Computational Fluid Dynamics. The work begins with the validation of the CFD method using a 6:1 prolate spheroid. The validated method is then employed for the study of the flow around a shape similar to the Airlander aircraft of Hybrid Air Vehicles Ltd. An overview of the flow around is presented, supported by pressure survey, flow visualisation and transitional flow effects. The sensitivity of the transition location to the Reynolds number is also demonstrated, and the role of each component of the vehicle is analysed in terms of its effect on the flow-field, the lift and drag, and stability in pitch. It was found that the fins contributed the most to increase the lift and drag coefficients.

1. Introduction

The study of lighter than air (LTV) and hybrid air vehicles[3] (HAV) involves several challenges. Firstly, this type of vehicles are characterised by flying at low speeds, while having very high Reynolds number (*Re*). In both the wind tunnel and CFD aerodynamic studies of these type of aircraft, *Re* is a key issue, as it can change up to two orders of magnitude from wind tunnel model-scale to full-scale aircraft. Since favourable pressure gradients are present in the vehicle's surface, the boundary layer stays laminar longer. In addition, due to the airframe shape, there is flow separation at the rear of the vehicle.

Over the past years, a few projects have been undertaken on the development of LTV technology. One example is the ZHIYUAN-1 stratospheric airship[27] developed in China. In the UK, the YEZ-2A project[12] was launched to demonstrate the capability of airships as airborne early warning systems for the US Navy. Currently, the LOCATE project (Collaborative industrial research into technology and manufacturing capability of Low Carbon aircraft using lighter than air Technology) is aiming to innovative novel configuration of LTV vehicles.

Computational Fluid Dynamics (CFD) is also emerging as a tool for the design and optimisation of LTV. Suman et al.[24] studied the bare hull of the ZHIYUAN-1 stratospheric airship[27] with the unstructured TAU solver of DLR. They used the Reynolds Averaged Navier-Stokes (RANS) equations and fixed the transition point by suppressing the turbulence model in the laminar flow region. Sensitivity studies on the transition location showed a decrease in drag when transition was moved downstream by up to 75% L. From that point, the drag increased with distance, due to flow separation. The numerical results with fixed transition at 52% L agreed broadly with the experimental data for angles of attack up to 5 deg. However, poor agreement was found for free-transition cases and for those with fixed transition at angles of attack higher than 5 deg. These discrepancies were attributted to the RANS method failing to resolve some of the relevant turbulence scales. Dumas et al.[9] presented prelimary CFD analyses of an open volume airship concept within the MAAT (Multibody Advanced Airship for Transport) project.

For validation and development of numerical methods related to LTVs, prolate spheroids have been extensively employed. Experimental data is availabe in the open literature for a 6:1 prolate spheroid[28] for a wide range of flow conditions and for a 3:1 prolate spheroid.[7] Sorensen[22] employed the 6:1 prolate spheroid[28] for the validation of the $\gamma - Re_\theta$ transition model, for Reynolds numbers between 3.2 and 9.6 million and at zero and 30 degrees of pitch. For the surface pressure, fully turbulent and transitional cases showed good agreement with the experiments. Although at zero pitch the transition model agreed better with the experimental friction coefficient than the fully turbulent case, the $\gamma - Re_\theta$ model was not able to predict the correct location of transition at a pitch of 30 deg. This was attributed to the

Copyright © 2015 by [M. CARRION, M. BIAVA, R. STEIJL, G.N. BARAKOS, D. STEWART]. Published by the EUCASS association with permission.

lack of cross-flow transition prediction capability of the employed transition model. Similar studies were performed by other authors.[8,26] In the case of airships, the 6:1 prolate spheroid was also employed to approximate the shape of the hull by Omari et al.[18,19]

To the best of the authors' knowledge, a CFD study of the complete configuration of an LTV or HAV has not been presented in the literature. Hence, after validating the employed CFD methods of Hybrid Air Vehicles Ltd., the present paper provides a study of the aerodynamics for an early variant of the Airlander HAV.

2. Numerical Method

The Helicopter Multi-Block (HMB2) CFD solver,[2] developed at Liverpool, is used for the present work, and has so far been validated for a number of applications, including helicopters, wind turbines, turboprop and UCAV aircraft. HMB2 solves the Navier-Stokes equations in integral form using the Arbitrary Lagrangian Eulerian (ALE) formulation for time-dependent domains with moving boundaries:

$$\frac{d}{dt}\int_{V(t)} \vec{\mathbf{w}} dV + \int_{\partial V(t)} \left(\vec{F}_i\left(\vec{\mathbf{w}}\right) - \vec{F}_v\left(\vec{\mathbf{w}}\right)\right)\vec{n} dS = \vec{S} \tag{1}$$

where $V(t)$ is the time dependent control volume, $\partial V(t)$ its boundary, $\vec{\mathbf{w}}$ is the vector of conserved variables $[\rho, \rho u, \rho v, \rho w, \rho E]^T$. $\vec{F}_i$ and $\vec{F}_v$ are the inviscid and viscous fluxes, including the effects of the mesh movement.

The Navier-Stokes equation are discretised using a cell-centred finite volume approach on a multi-block grid, leading to the following equations:

$$\frac{\partial}{\partial t}\left(\mathbf{w}_{i,j,k} V_{i,j,k}\right) = -\mathbf{R}_{i,j,k}\left(\mathbf{w}_{i,j,k}\right) \tag{2}$$

where $\mathbf{w}$ represents the cell variables and $\mathbf{R}$ the residuals. i, j and k are the cell indices and $V_{i,j,k}$ is the cell volume. Osher's[20] upwind scheme is typically used for the discretisation of the convective terms and MUSCL[25] variable extrapolation is used to provide a formally 3rd order accurate scheme. To account for low-speed flows, the Low-Mach Roe scheme (LM-Roe) developed by Rieper[21] is employed.[4] The linearised system is solved using the generalised conjugate gradient method with a block incomplete lower-upper (BILU) pre-conditioner.[1] The HMB2 solver has a library of turbulence closures which includes several one- and two- equation turbulence models and versions of the $k-\omega$ model, including the recently developed Scale-Adaptative Simulation (SAS) model,[16] and the $\gamma - Re_{\theta_t}$ transition model.[29]

3. Mesh Generation

Multi-block structured topologies were employed, to allow for a good representation of the arship surface. The blocks were also used for balancing the computational load between processors for parallel computing. Since the vehicle is symmetric with respect to the XZ plane, only half of the vehicle was meshed, assuming symmetry. This reduced the size of the grid by half and therefore enabled savings on computational resources. Nevertheless, some cases were computed on the full mesh to ascertain that the symmetry assumption appears to be valid if the flow yaw angle is zero. At the inflow, outflow and far-field boundaries free-stream conditions were assumed, as shown in Figure 1 (a). Both inflow and far-field were located at 5L from the vehicle and the outflow boundary was located at 8L.

A set of five sliding planes[23] were employed, to allow for localised grid refinement near the body and to have a cartesian grid in the rest of the domain. These planes are the ones close to the body presented in Figure 1 (a). An O-topology was employed around the Airlander, for optimal orthogonality of the cells to the surface, see Figure 1 (b). A first cell size of 3μm was employed, to ensure a y^+ of < 1.

Table 1: Summary of mesh properties.

Grid ID	Components	Size (Blocks)	Cross sect.-(span)-wise cells	Boundary layer cells
AL 1	Bare Hull	9.2M (1,069)	236 (314)	34
AL 2	Hull & Fins	9.5M (1,151)	236 (314)	34
AL 3	Hull, Fins & LERX	10.8M (1,203)	236 (314)	34
AL 4	Hull, Fins, LERX & Strakes	10.8M (1,203)	236 (314)	34
AL 5	Refined **AL 4**	28.4M (1,253)	456 (410)	60

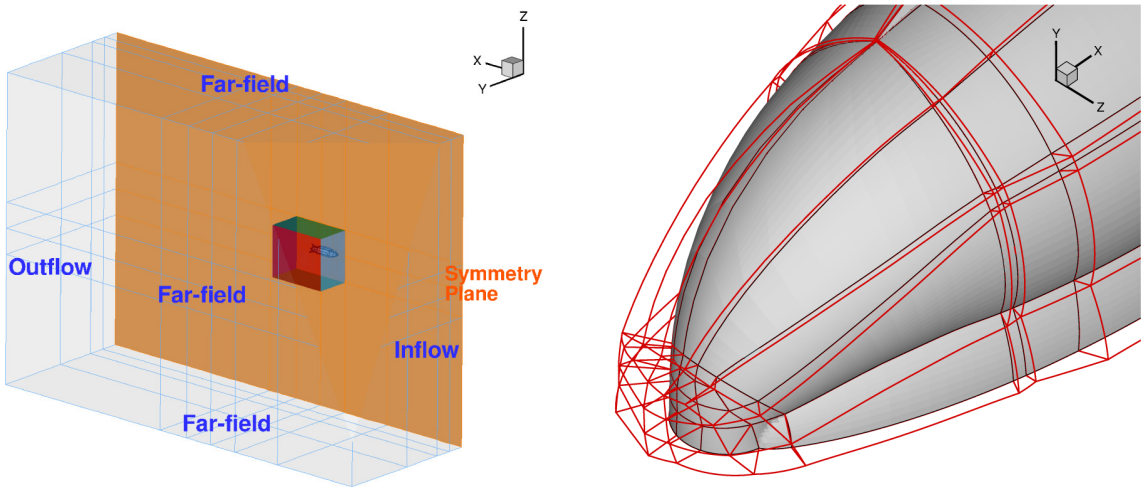

(a) Domain extension and boundaries. **(b)** O-topology around the body.

Figure 1: Overview of the multi-block topology for the Airlander.

Four configurations were considered for the Airlander vehicle, which are shown in Figure 2 and whose properties are summarised in Table 1 . **AL 1** consists of the bare hull; the fins were then added (**AL 2**) and also the leading edge extension (LERX) in configuration **AL 3**. Finally, the strakes were considered in configuration **AL 4**. To assess grid convergence, two grid refinements were employed for the baseline case (grids **AL 4** and **AL 5**).

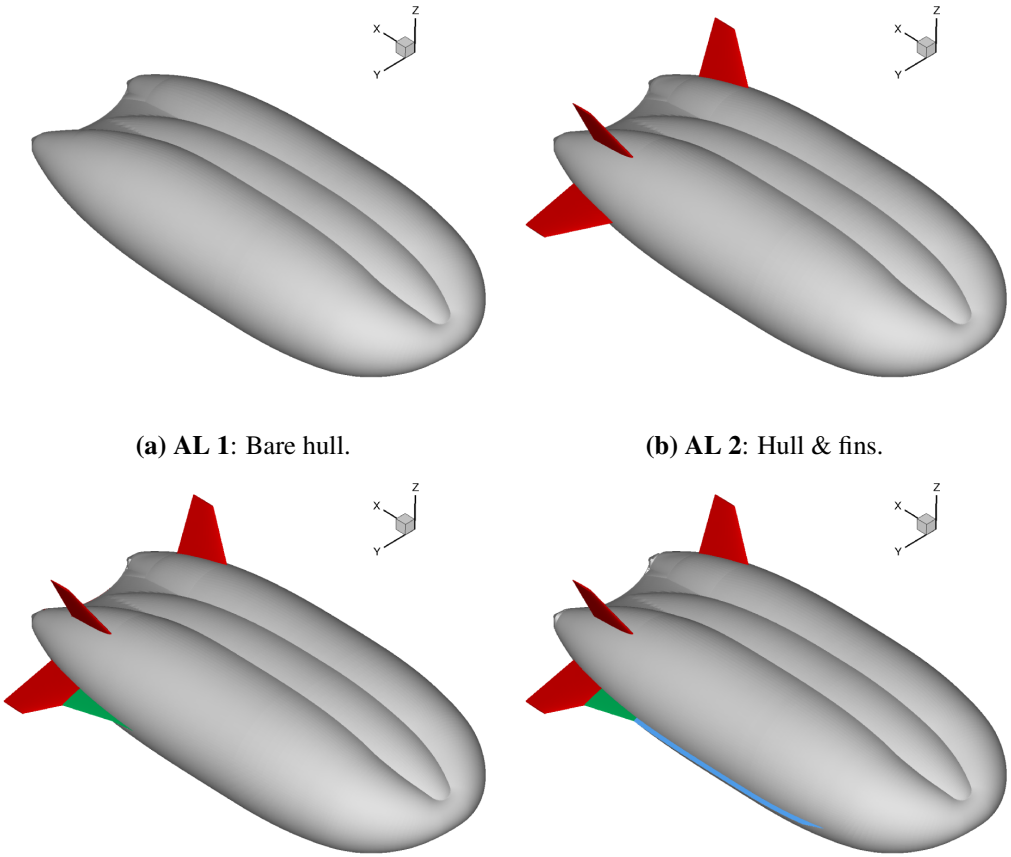

(a) AL 1: Bare hull. **(b) AL 2**: Hull & fins.

(c) AL 3: Hull, fins & LERX. **(d) AL 4**: Hull, fins, LERX & strakes

Figure 2: Vehicle configurations.

4. Results and discussion

The computational results are presented in this section. Since no experimental data is available for the Airlander, as an early stage design was employed, and the hull has some resemblance to a spheroid, the 6:1 prolate spheroid[6] was employed for the validation of the method. A 20-degree pitched case was studied, at Reynolds number of 4.2 million and Mach number of 0.15. A number of computations are then presented for the approximate Airlander (AL), including the role of the strakes in the aerodynamic coefficients and effect of the flow conditions and Reynolds number on the transition onset. In all cases, a wind speed of 40m/s was employed and sea level flow conditions were assumed. Unless otherwise specified, the Reynolds number, based on the vehicle's length (L), was 3 million. RANS and URANS computations were performed, with the k-ω SST turbulence model by Menter.[15]

4.1 Validation of the method

For the 6:1 prolate spheroid,[6] an O-topology was employed for the grid of 40 million cells. Two main counter-rotating vortices are generated, as can be seen in the contours of the $Q-$criterion[14] of Figure 3 (a). A secondary vortex is also captured, located at an azimuth of 140 degrees, which is in good agreement with experiments.[6]

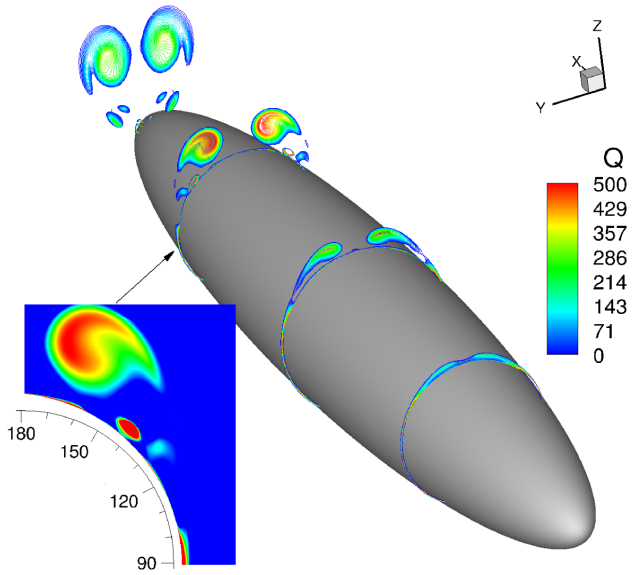

(a) Contours of $Q-$criterion,[14] with detail at $x = 77\%$L.

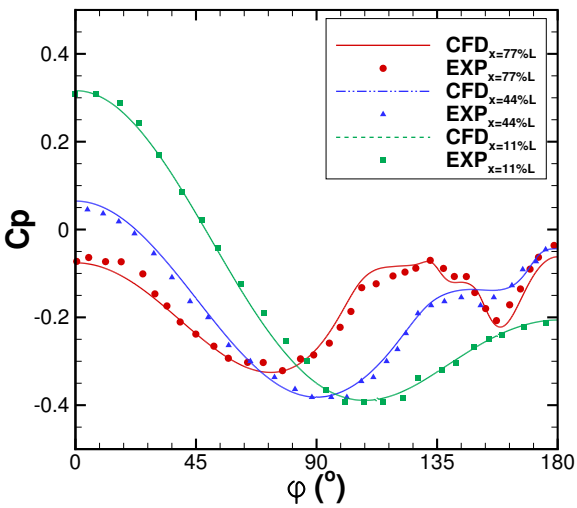

(b) Pressure coefficient at three axial stations.

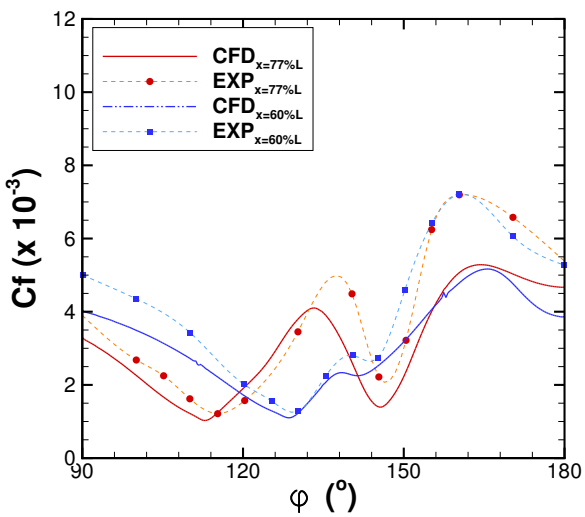

(c) Friction coefficient at two axial stations.

Figure 3: Flow around a 6:1 prolate spheroid at $\alpha = 20°$, $M_\infty = 0.15$ and $Re = 4.2 \cdot 10^6$.

The correct prediction of the flow can also be seen in the surface pressure coefficient distribution of Figure 3 (b). At x = 77%L, the presence of the second vortex very close to the spheroid surface leads to a drop in pressure, with very good agreement with the experimental data published by Wetzel et al.[28] In the case of the friction coefficient (C_f) presented in Figure 3 (c), the experiments by Chesnakas et al.[6] were used. In this case, reasonable agreement with experiments was obtained, with good C_f predictions from 90 to 150 deg. of azimuth and slightly under-prediction from 150 to 180deg. Similar agreement was obtained to other works presented in the literature,[8] who also predicted less peak-to-peak variation, even though they employed different turbulence models (RANS and DES with Spalart-Allmaras). These discrepancies in friction could be due to difficulties of the turbulence models to predict the evolution of the vortical structure, which seems to be weaker in the CFD, but also difficulties in the experiment to measure these quantities with high level of accuracy. Nevertheless, the CFD predicted successfully the trend and overall level of the experimental data.

Figure 4 shows contours of helicity on a slice at $x = 77\%L$. For these flow quantities, good agreement with the experiments[6] is also observed.

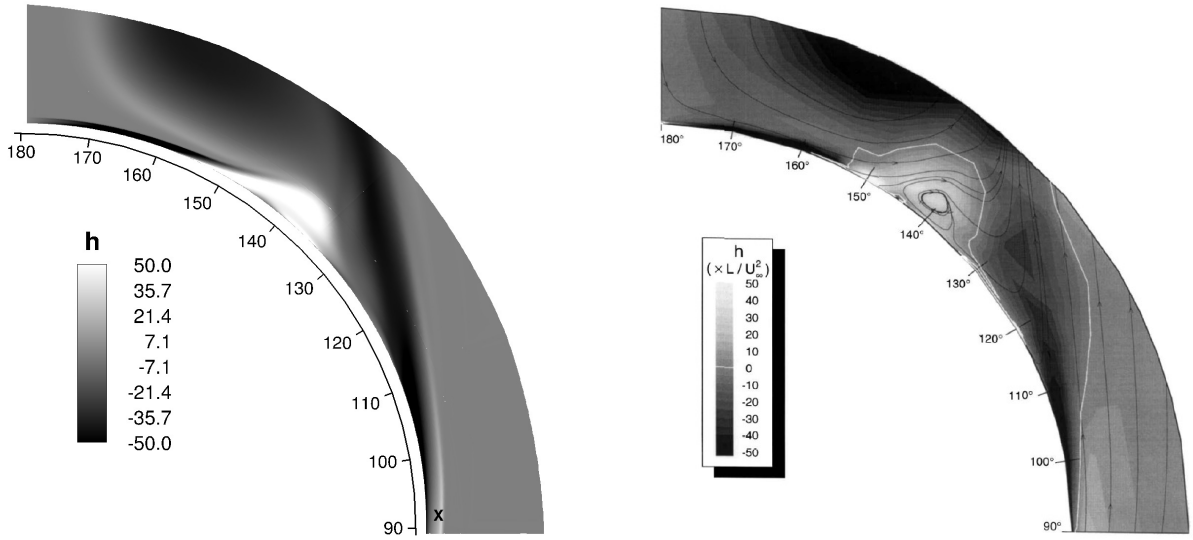

(a) CFD. **(b)** Experiments.[6]

Figure 4: Contours of helicity at $x = 77\%L$ on a 6:1 prolate spheroid.

4.2 Flow topology around an airship

Results for the flow around the 'AL' are presented in this paragraph, including the surface pressure, vortex generation and transition effects.

4.2.1 Pressure field analysis

A comparison is first shown between the **AL 4** and **AL 5** cases of Table 1. The pressure coefficient (C_p) at the symmetry and mid-planes are presented in Figure 5. The solutions are practically the same, with small differences close to the back of the vehicle. Grid convergence can therefore be assumed, with the employed URANS framework.

As can be observed in Figure 5, favourable pressure gradients ($\partial p/\partial s < 0$) are present from the nose to 25% L, which indicates fully attached flow. From 25 to 80% L, a neutral pressure gradient ($\partial p/\partial s \approx 0$) is present in both upper and lower surfaces. From 80% L, the adverse pressure gradient ($\partial p/\partial s > 0$) leads to flow separation.

4.2.2 Flow visualisation

Figure 6 shows the vortices generated by the different components of the airship, for 10 and 20 degrees of pitch. As can be observed, a clock-wise vortex is firstly formed by the strake (**A**), see Figures 6 (a) and (d), with higher strength at higher pitch angles. Additionally, the curvature of the hull leads to the creation of an upper vortex (**B**), that appears at x = 0.60L, approximately. This is more obvious for the 20-degree pitched case.

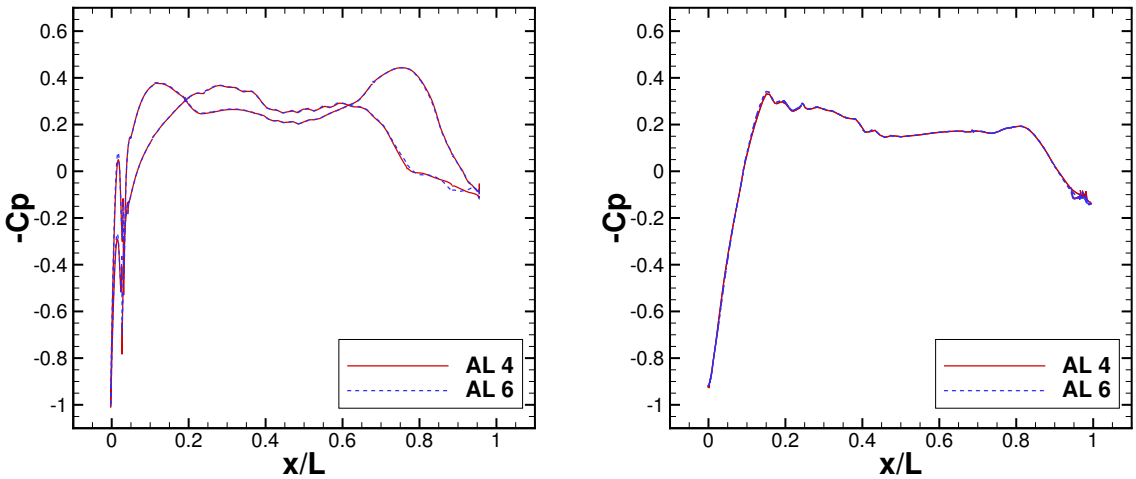

(a) Symmetry plane.

(b) Mid-plane.

Figure 5: Effect of the mesh density in the C_p. of the approximated Airlander.

Moving further downstream at $x = 0.85$L (Figures 6 (b) and (e)) the strake vortex (**A**) becomes bigger due to the presence of the LERX, and eventually merges with the vortex generated by the lower fin (**D**). A second and a third vortex are also generated by the hull. The second one (**C**) is generated between the upper and lower fins and can be clearly identified in Figure 6 (e). This vortex is shed downstream and is seen in Figure 6 (f) in the ones with high vorticity magnitude on the left side. The third one is generated on the lower surface of the vehicle.

The tips of the upper fins also generate vortices (**E**), which can be seen in Figures 6 (c) and (f). Since the vortices of the upper and lower fins are co-rotating, they interact and eventually merge further downstream.

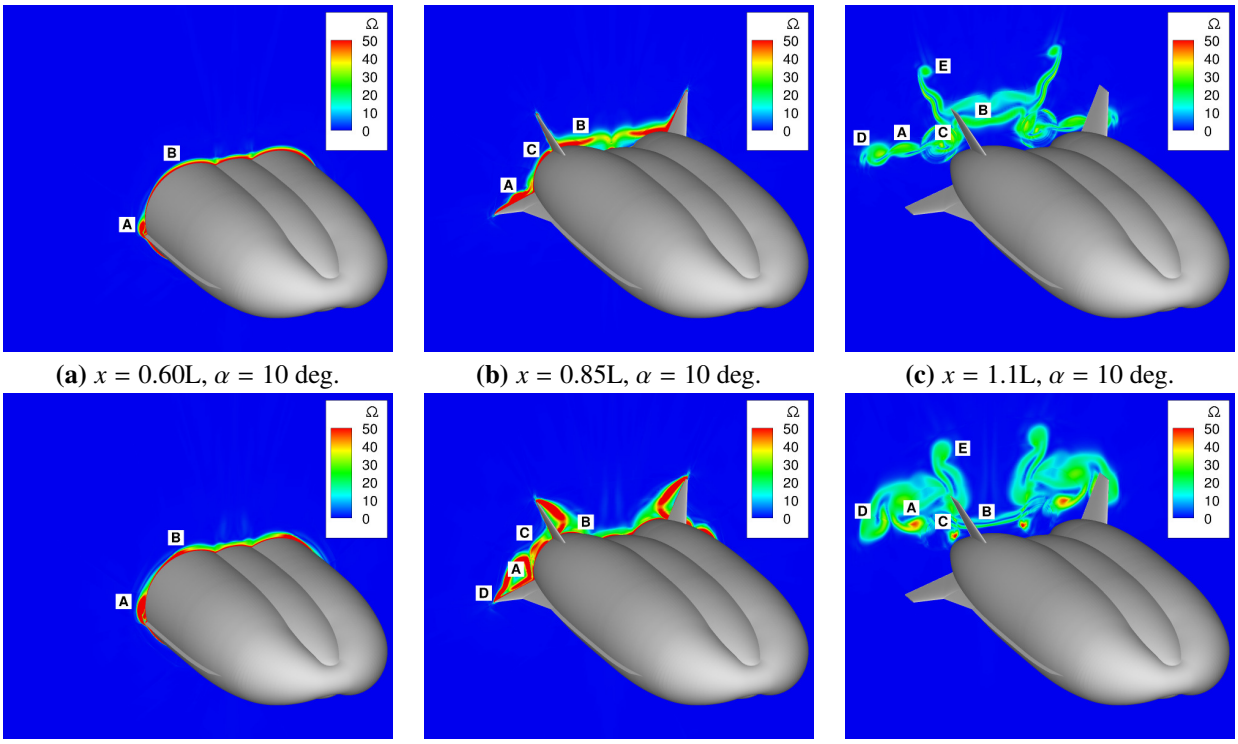

(a) $x = 0.60$L, $\alpha = 10$ deg.

(b) $x = 0.85$L, $\alpha = 10$ deg.

(c) $x = 1.1$L, $\alpha = 10$ deg.

(d) $x = 0.60$L, $\alpha = 20$ deg.

(e) $x = 0.85$L, $\alpha = 20$ deg.

(f) $x = 1.1$L, $\alpha = 20$ deg.

Figure 6: Visualisation of the flow around the approximated AL body with vorticity magnitude.

4.3 Transition effects

The location of the transition onset on the AL body is estimated, employing empirical criteria and fully turbulent CFD results. For this, Michel's[17] and Cebeci and Smith's criteria[17] are employed on streamlines extracted in the boundary layer of each of the computations. These two methods are based on experimental data on flat plates and aerofoils and provide an estimate of the location of the transition onset when the local momentum thickness Reynolds number ($Re_{\theta,tr}$) reaches a particular value. In the case of Michel's criterion,[17] the transition onset location takes place when

$$Re_{\theta,tr} \approx 2.9 Re_{x,tr}^{0.4}, \tag{3}$$

where $Re_{x,tr}$ is the Reynolds number, based on the distance measured from the stagnation point. In Cebeci and Smith's correlation,[5] the transition is located at the point where

$$Re_{\theta,tr} = 1.174\Big(1 + \frac{22400}{Re_{x,tr}}\Big) Re_{x,tr}^{0.46}. \tag{4}$$

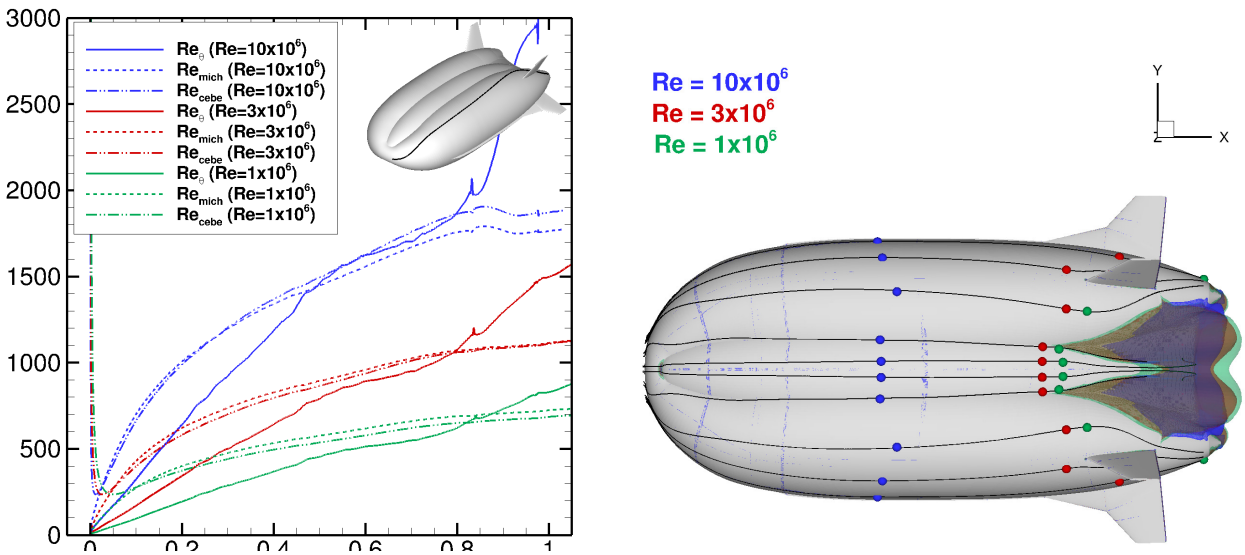

(a) Empirical transition criteria.

(b) Transition onset and iso-surfaces of reverse flow.

Figure 7: Sensitivity of the transition onset to the Reynolds number.

Figure 7 shows the momentum thickness Reynolds number (Re_θ) along a streamline of the CFD solution and the empirical transition criteria, where changes in Reynolds number were considered. At Re = 3 million, the presence of favourable pressure gradients make the boundary layer to stay laminar until 80% L, approximately. When the Reynolds number is reduced, the boundary layer becomes less turbulent. The opposite effect happens when the Reynolds number increases. The transition onset is moved downstream and upstream, for lower and higher Reynolds respectively. When the Reynolds number was reduced by a third, the transition onset was moved downstream by 5% L, approximately. When it was increased from 3 to 10 million, the transition onset moved upstream by 42% L. These results show the strong effect on the Reynolds number to the nature of the boundary layer.

As can be seen in the iso-surfaces of reversed flow of Figure 7 (b), when the Reynolds number is higher (and therefore the upstream boundary layer is more turbulent), the region of separated flow is smaller. Conversely, at lower Reynolds number the flow tends to separate more.

4.4 Study of the role of the components

To quantify the role of each of the components of the 'AL' airship, cases **AL 1** to **AL 4** of Table 1 are compared in this section. For this, the flow is firstly analysed and sensitivity studies on the loads and stability are provided.

4.4.1 Role of the airship components

Figure 8 shows the vortex downstream the vehicle (at $x = 1.05L$), with contours of vorticity magnitude (Ω), at 20 degrees of pitch. For the bare hull, only two vortices (**A**) are shed (Figure 8 (a)), that rotate clock-wise and which are due to the curvature of the hull. Two vortices are shed by the tips of the fins (one for the upper (**B**) and another one for the lower (**C**)), see Figure 8 (b). The LERX provides an extra disturbance that merges with the one created by the lower fin (**C+D**), as can be seen in Figure 8 (c). The strakes generate another vortex, that blends with the one generated by the fin (**C+D+E**), since they are co-rotating, see Figure 8 (d).

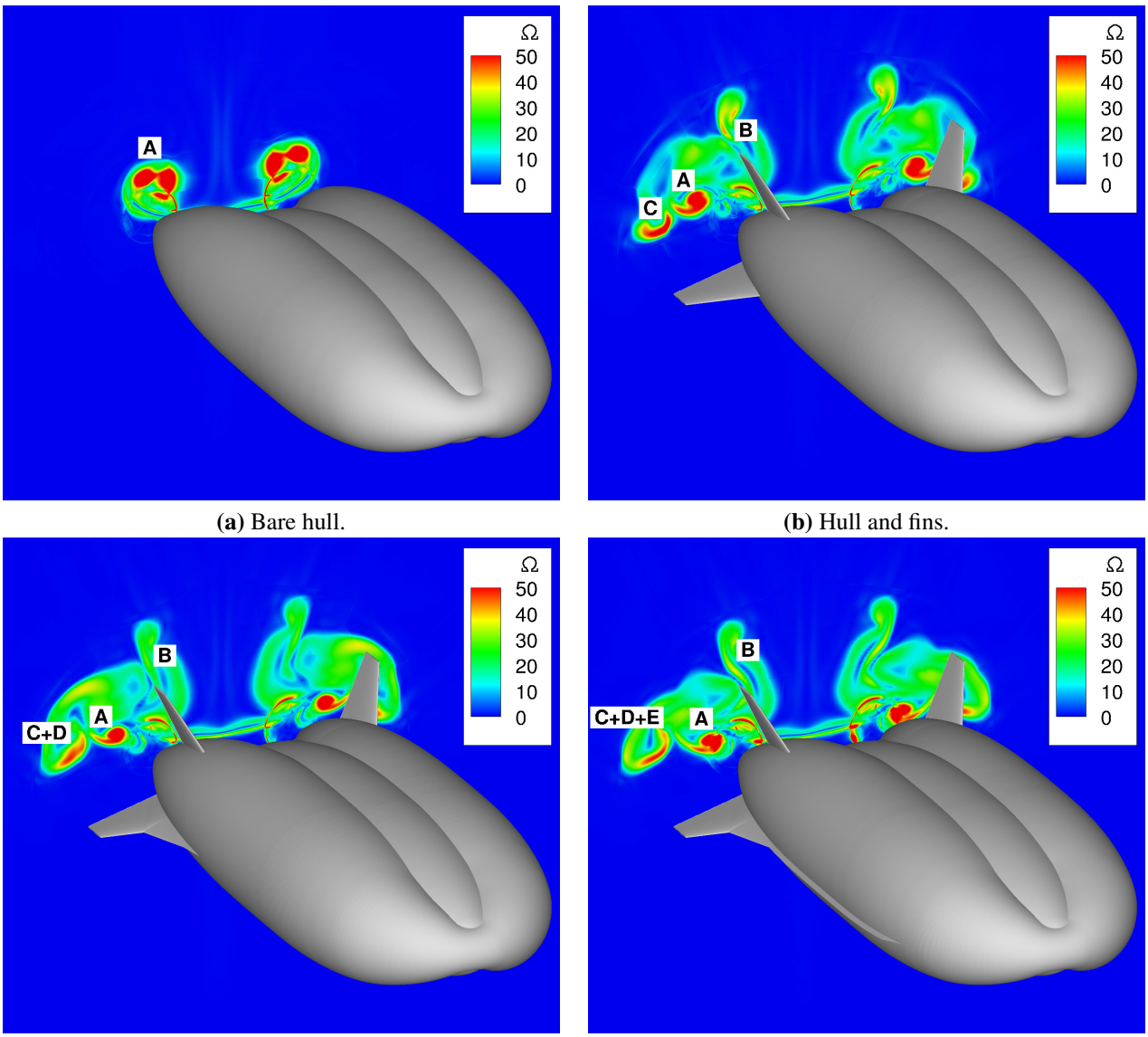

(a) Bare hull.

(b) Hull and fins.

(c) Hull, fins and LERX.

(d) Hull, fins, LERX and strakes.

Figure 8: Contours of vorticity magnitude for different vehicle configurations.

The vortices generated on the baseline strakes at different pitch angles (visualised with streamlines) are presented in Figure 9. At higher pitch angles the vortices are stronger and longer as observed by the streamlines. On the other hand, at negative pitch the vortex is shed towards the low side of the strake, therefore reducing the lift.

4.4.2 Role of the components on the loads and pitch stability

Figures 10 (a) and (b) show the polars of lift and drag coefficients (based on the vehicle's volume) and Figure 10 (c) presents the lift-drag ratio. Note that all computations were run as steady-state. The highest pitch angle case (α =20 deg.) was computed steady and unsteady and the same aerodynamic coefficients were obtained. Figure 10 therefore

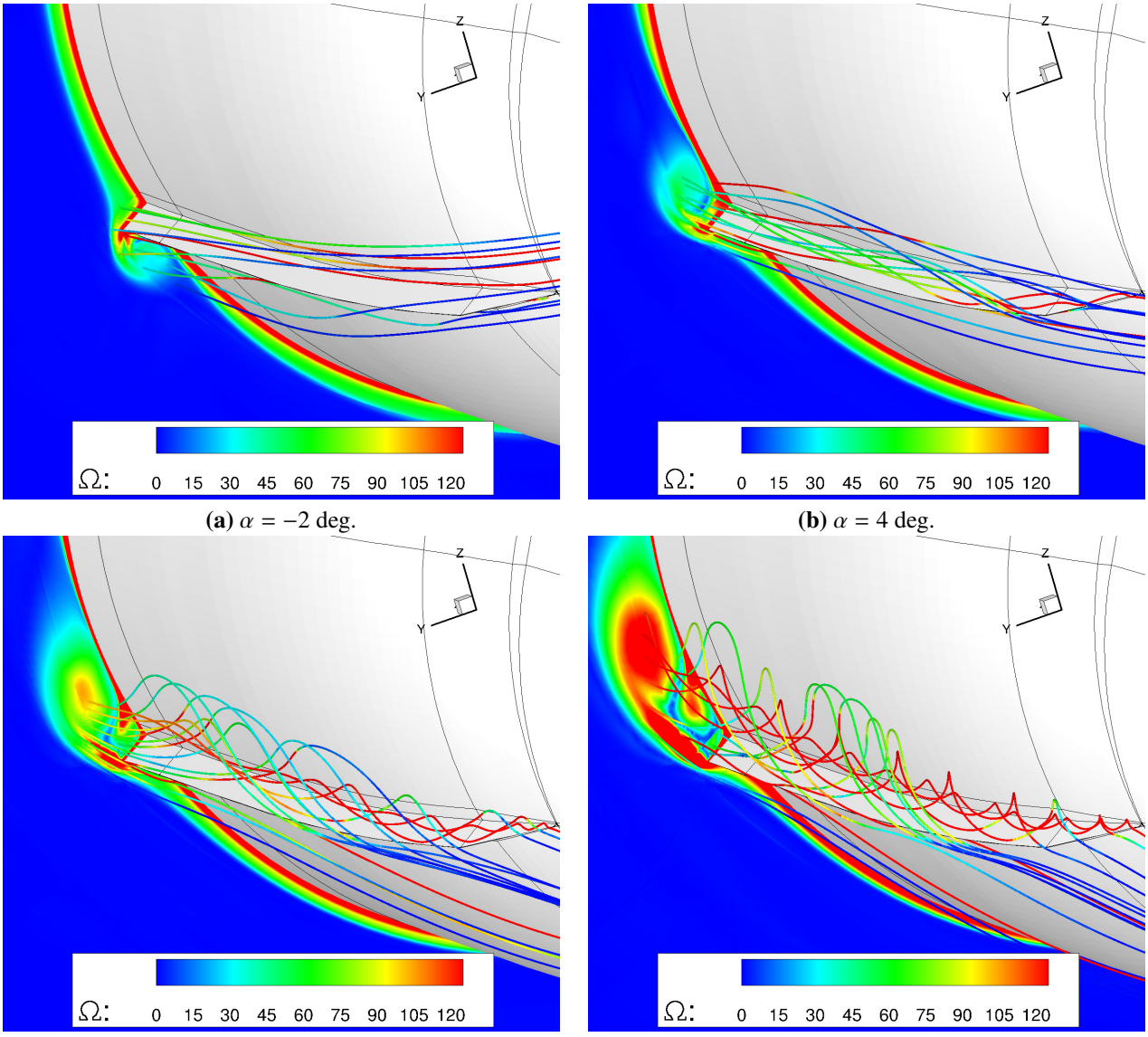

(a) $\alpha = -2$ deg. **(b)** $\alpha = 4$ deg.

(c) $\alpha = 10$ deg. **(d)** $\alpha = 20$ deg.

Figure 9: Vortex generated by the baseline strake visualised with flow streamlines.

shows that for the studied range of pitch angles, steady computations can be employed, since there is agreement between the RANS and URANS solutions.

For conventional and hybrid airships, the zero-lift drag coefficient ($C_{DV_{(H)}}$) is typically estimated employing Hoerner's[13] equation:

$$C_{DV_{(H)}} = C_F \cdot \left[4 \cdot \left(\frac{l}{d}\right)^{1/3} + 6 \cdot \left(\frac{d}{l}\right)^{1.2} + 24\kappa \cdot \left(\frac{d}{l}\right)^{2.7}\right]. \tag{5}$$

In equation (5), the first term in the right hand side corresponds to the friction drag; the second term is pressure drag; the third one is the drag due to separation. For the friction coefficient (C_F), Schoenerr's[13] formula presented in eq. (6) is employed, which is only dependent on the Reynolds number (Re).

$$C_F = \frac{1}{(3.46 \cdot Log_{10}Re - 5.6)^2}. \tag{6}$$

It should be noted, however, that the l/d ratio for airships is difficult to define, since it is not perfectly cylindrical. Here, the reference diameter (d) was chosen as the equivalent one of a circle with the same area as the cross-section of the vehicle at mid-span.

As can be seen in Figure 10 (a), for the design employed in the present paper, zero lift is achieved at 5 deg. of pitch. For this angle, there is reasonable agreement of the drag coefficient with the theory, as shown in Figure 10 (b), although the theory gives lower drag as is strictly applied to spheroids.

For positive angles, the components increase the lift and also the drag, which is more obvious at high pitch angles. For example, at 20 degrees of pitch, the lift and drag increased by 56.3% and 34.5%, respectively. This means that at that α, more than half of the overall lift generated by the vehicle is due to the fins, LERX and strakes. Conversely, at negative pitch angles these components contribute to reduce the lift.

The lift-drag ratio reaches a peak at $\alpha = 12$ deg. with a value of 2.6 for the bare hull case and 3.8 for the full vehicle. Although at high pitch angles the components increased the lift considerably, as shown in Figure 10 (a), the drag increased further (see Figure 10 (b)). The L/D therefore increased by almost 160% at $\alpha = 4$ deg., but only by 16.5% at $\alpha = 20$ deg. This shows that the aerodynamic components are less effective for pitch angles higher than 12 deg.

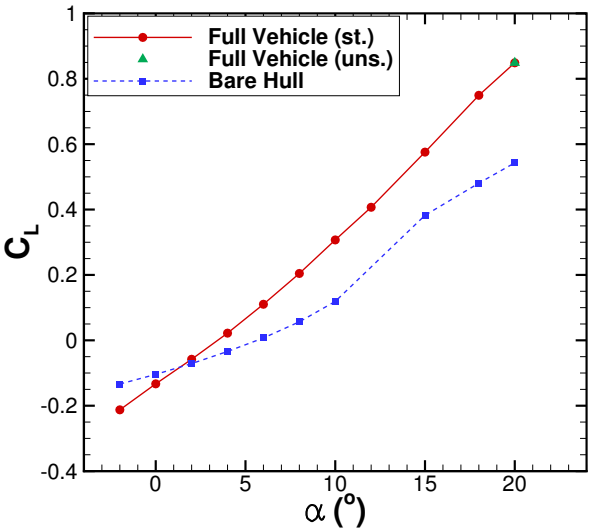

(a) Lift coefficient.

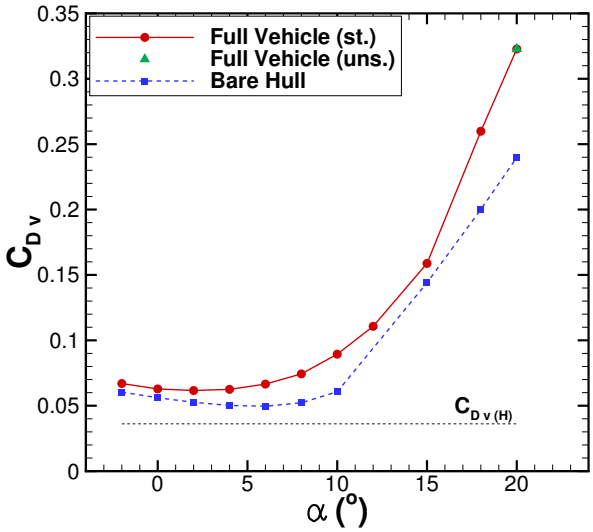

(b) Drag coefficient.

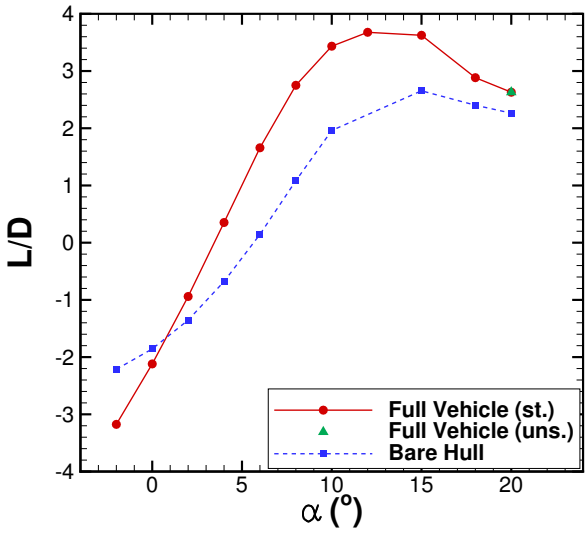

(c) L/D ratio.

Figure 10: Polars of lift and drag, and L/D ratio (st.: steady, uns.: unsteady).

Figure 11 shows slices at the hull's symmetry and mid-planes for the bare hull and the full vehicle configurations, for 20 deg. of pitch. As can be observed, at the symmetry plane (Figure 11 (a)), the pressure at the hull is mainly affected by the fins at the back. For the mid-plane slice of Figure 11 (b), a significant change in the pressure is observed due to the vortex generated by the strakes that affects the boundary layer of the hull. Likewise, the LERX and fins also

change the pressure profile. This can be better observed in the pressure coefficient contours of Figure 12, where there is a trace of suction on the hull due to the presence of both the LERX and strake.

This shows that not only the different components contribute to a change on loads, but also the contribution of the hull itself changes, due to the interaction.

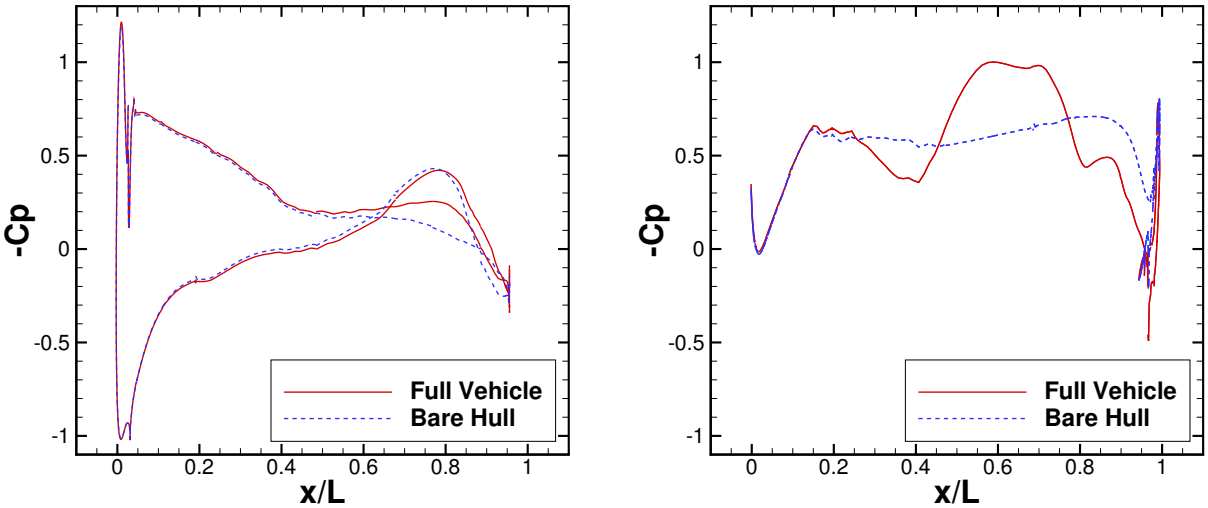

(a) Symmetry plane.

(b) Mid-plane.

Figure 11: Effect of the components on the the pressure coefficient (C_p) on the hull, at 20deg. of pitch.

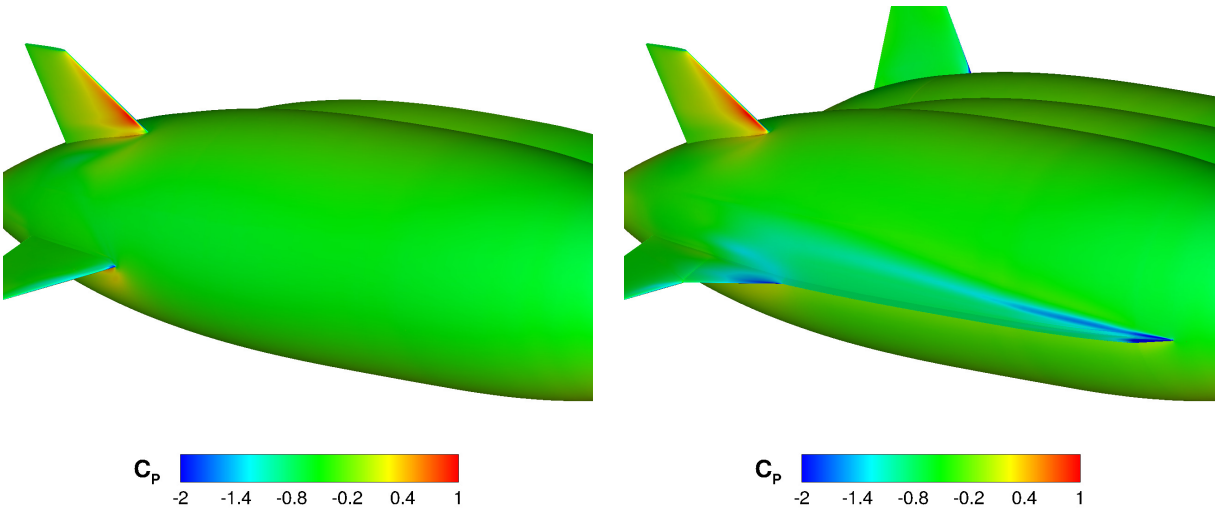

(a) Fins only.

(b) Fins, LERX and strakes.

Figure 12: Contours of pressure coefficient (C_p) on the surface of the vehicle, at 20deg. of pitch.

To assess which components are the ones contributing the most to the overall lift and drag, Figure 13 shows the relative changes with respect to the bare hull case (**AL 1**) for the four vehicle configurations presented in Figure 2, at 10 and 20 degrees of pitch. At 10 deg. of pitch, as presented in Figure 13 (a), the fins increased the lift by more than twice and the LERX and strakes contributed to a further small increase. The drag also increased when each component was considered, but in less percentage. As Figure 13 (b) shows, at 20 deg. of pitch, the increase in loads is not as drastic as in the previous case. The fins increased the lift by less than 50% and the strakes seem to provide more lift than the LERX. In this case, the penalties in drag were closer to the increase in drag than at in the previous case.

These results show that with the presented configuration of the approximated Airlander, the fins are the components that contribute the most to the lift and also drag.

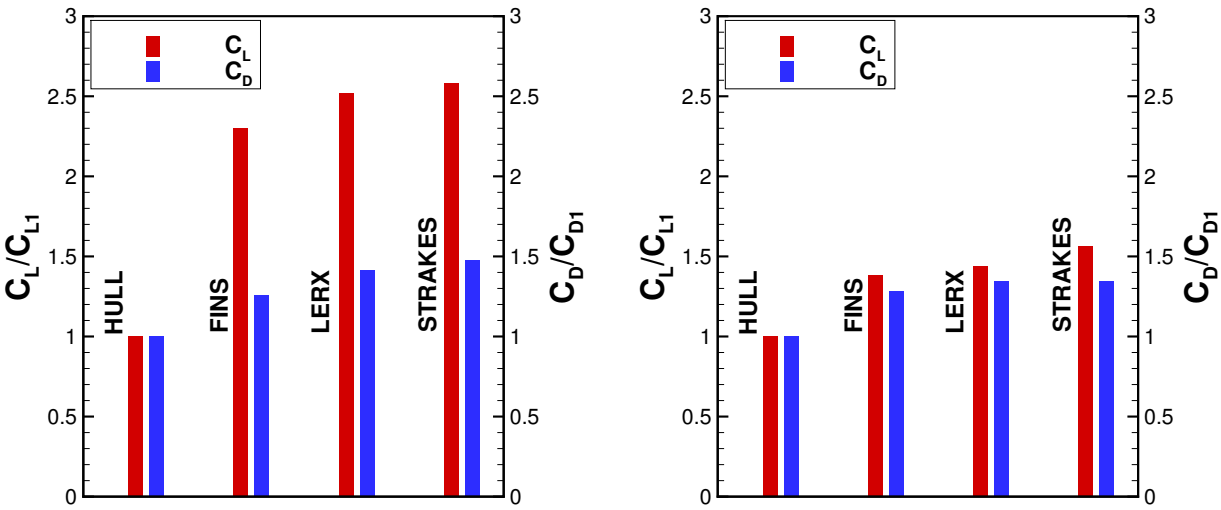

(a) α = 10 deg. **(b)** α = 20 deg.

Figure 13: Contribution of each component to the lift and drag, with respect to the bare hull configuration.

Regarding the stability of the vehicle, the pitching moment (C_{M_y}) and the change of it with the pitch angle (C_{M_α}), calculated at the center of volume, are presented in Figure 14. Positive C_{M_α} means nose up attitude and negative is nose down. As Figure 14 (b) shows, both bare hull and full configurations seem to be unstable, as the tendency of the vehicle is to pitch up for positive changes in pitch. This should be attributed to the fact that no buoyancy force was included in the computations. Similar behaviour was observed in other works in the literature that did not account for buoyancy effects. This is the case of the experiments on the AKRON,[10] YEZ-2A[12] and ZHIYUAN-1[24,27] airships, that also presented positive C_{M_α}.

Nevertheless, the presence of the aerodynamic components has a stabilising effect, since there is a reduction in the pitch derivative. This was also seen by Wang *et al.*[27] and Freeman.[10] In addition, since the 'AL' is not axisymmetric, at zero pitch angle the pitching moment is not zero, which differs from more traditional airship configurations.[11,12,24,27]

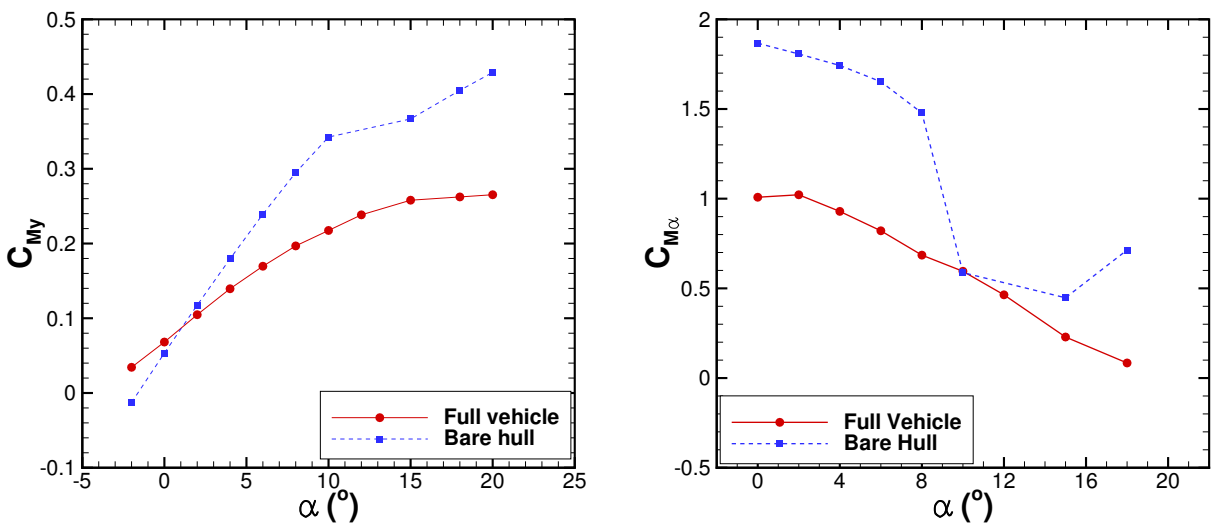

(a) Pitching moment. **(b)** Derivative of pitching moment.

Figure 14: Pitching moment (C_{M_y}) and derivative (C_{M_α}) at the center of volume.

5. Conclusions

The employed CFD method (HMB2) was validated for the 6:1 prolate spheroid, and showed good agreement with the experiments.

The flow around an early design of the Airlander aircraft was analysed, and the body vortices were identified. Due to the presence of favourable pressure gradients, the onset of transition was predicted close to the rear of the airship, at 80% L. Sensitivity studies on the Reynolds number showed a further downstream transition onset for lower Reynolds numbers and an increase of Reynolds led to an earlier transition onset.

The study continued by exploring the role of each component of the airship on the aerodynamic coefficients and the stability derivatives. The results showed that with the standard vehicle configuration, the fins contributed the most to an increase in lift and also drag.

In the future, further work is planned on the transitional flow effects, as well as further validation of the HMB2 method.

Acknowledgements
The computations were performed on the N8 HPC facility "Polaris" at Leeds University and the Chadwick cluster of the University of Liverpool. Access to both systems is gratefully acknowledged, as well as the financial support by the LOCATE Project.

References

[1] O. Axelsson. *Iterative Solution Methods*. Cambridge University Press: Cambridge, MA, 1994.

[2] G. Barakos, R. Steijl, K. Badcock, and A. Brocklehurst. Development of CFD capability for full helicopter engineering analysis. In *31st European Rotorcraft Forum, Florence, Italy*, 2005.

[3] G.E. Carichner and L.M. Nicolai. Hybrids...the airship messiah? In *Proceedings of the AIAA Lighter-Than-Air Systems Technology Conference*, Daytona Beach, Florida, USA, March 2013.

[4] M. Carrión, M. Woodgate, R. Steijl, and G. Barakos. Implementation of All-Mach Roe-type Schemes in Fully Implicit CFD Solvers - Demonstration for Wind Turbine Flows. *International Journal for Numerical Methods in Fluids*, 73(8):693–728, 2013.

[5] T. Cebeci and A. M. O. Smith. *Analysis of Turbulent Boundary Layers*. Number 15. Applied Mathematics and Mechanics. Academic Press, New York, NY, 1974.

[6] C.J. Chesnakas and R. Simpson. Detailed Investigation of the Three-Dimensional Separation About 6:1 Prolate Spheroid. *AIAA Journal*, 35(6):990–999, June 1997.

[7] D.B. Clarke, P.A. Brandner, and G.J. Walker. Experimental and Computational Investigation of Flow Around a 3:1 Prolate Spheroid. *WSEAS Transactions of Fluid Mechanics*, 3(3):207–217, July 2008.

[8] G. Constantinescu, H. Pasinato, Y. Wang, J. Forsythe, and K. Squires. Numerical Investigation of Flow Past a Prolate Spheroid. *Transactions of the ASME*, 124:904–910, December 2002.

[9] A. Dumas, M. Madonia, G. Ilieva, M. Trancossi, J. Pascoa, and A. Coppola. CFD Analysis and Optimization of a Variable Shape Airship. In *Proceedings of the ASME 2012 International Mechanical Engineering Congress and Exposition*, Houston, Texas, USA, November 2012.

[10] H.B. Freeman. Force Measurements on a 1/40-scale Model of the U.S. Airship 'AKRON'. *PhD Thesis, Cranfield Institute of Technology*, October 1990.

[11] P. Funk, T. Lutz, and S. Wagner. Experimental Investigations on Hull-Fin Interferences of the Lotte Airship. *Aerospace Science and Technology*, 7:603–610, 2003.

[12] S.B.V. Gomes. An Investigation of the Flight Dynamics of Airships with Application to the YEZ-2A. *PhD Thesis, Cranfield Institute of Technology*, October 1990.

[13] S.F. Hoerner. *Fluid-dynamic drag; practical information on aerodynamic drag and hydrodynamic resistance*. Midland Park, N. J., 1958.

[14] J. Jeong and F. Hussain. On the Identification of a Vortex. *Journal of Fluid Mechanics*, 285:69–94, 1995.

[15] F.R. Menter. Two-Equation Eddy-Viscosity Turbulence Models for Engineering Applications. *AIAA Journal*, 32(8):1598–1605, 1994.

[16] F.R. Menter and Y. Egorov. The Scale-Adaptive Simulation Method for Unsteady Turbulent Flow Predictions. Part 1: Theory and Model Description. *Flow Turbulence Combust*, 85:113 138, 2010.

[17] R. Michel. *Etude de la transition sur les profils d'aile, etablissement d'un critere de determination du point de transition et calcul de la trainee de profil incompressible*. Technical Report 1/1578A, 1951.

[18] K. Omari, E. Schall, B. Koobus, and A. Dervieux. Turbulence Modeling Challenges in Airship CFD Studies. *Monografías del Seminario Matemático García Galdeano*, 31:545–554, 2004.

[19] K. Omari, E. Schall, Y. Le Guer, and M. Amara. Numerical Study of Turbulent Flow Around a Generic Airship at High Angle of Attack. In *4th International Conference on Computational Heat and Mass Transfer*, Paris-Cachan, France, May 2005.

[20] S. Osher and S. Chakravarthy. Upwind Schemes and Boundary Conditions with Applications to Euler Equations in General Geometries. *Journal of Computational Physics*, 50(3):447–481, June 1983.

[21] F. Rieper. A low-Mach number fix for Roe's approximate Riemann solver. *Journal of Computational Physics*, 230:5263–5287, March 2011.

[22] N. Sorensen. CFD Modelling of Laminar-Turbulent Transition for Airfoils and Rotors Using the $\gamma - Re_\theta$ Model. *Wind Energy*, 12:715–733, April 2009.

[23] R. Steijl and G. Barakos. Sliding Mesh Algorithm for CFD Analysis of Helicopter Rotor-Fuselage Aerodynamics. *Int. J. Numer. Meth. Fluids*, 58:527–549, October 2008.

[24] S. Suman, S. Lakshmipathy, and R. Pant. Evaluation of Assumed-Transition-Point Criterion in Context of Reynolds-Averaged Simulations Around Lighter-Than-Air Vehicles. *Journal of Aircraft*, 50(2), March-April 2013.

[25] B. van Leer. Towards the Ultimate Conservative Difference Scheme, V. A Second Order Sequel to Godunov's Method. *J. Comp. Phys.*, 32:101–136, 1979.

[26] V. Vatsa, J. Thomas, and B. Wedan. Navier-Stokes Computations of a Prolate Spheroid at Angle of Attack. *Journal of Aircraft*, 26(11):986–993, 1989.

[27] X. Wang, G. Fu, P. D, and X. Shan. Experimental Investigations on Aerodynamic Characteristics of the ZHIYUAN-1 Airship. *Journal of Aircraft*, 47(4), July-August 2010.

[28] T. Wetzel. Unsteady Flow Over a 6:1 Prolate Spheroid. *PhD Thesis, Virginia Polytechnic Institute and State University*, 1996.

[29] G. Zografakis and G.N. Barakos. Transition Modelling for Rotorcraft CFD. 34th European Rotorcraft Forum, Liverpool, UK, September 2008. .